Colloidal fouling mitigation using pulsating flows in osmotic membrane processes

Andreas Kastl*, Alexander Präbst, Florian Kiefer, Markus Spinnler, Thomas Sattelmayer

Lehrstuhl für Thermodynamik, Technische Universität München Boltzmannstr. 15, 85748 Garching, Germany, Tel. +49 89 289 16252;
emails: kastl@td.mw.tum.de (A. Kastl), praebst@td.mw.tum.de (A. Präbst), kiefer@td.mw.tum.de (F. Kiefer),
spinnler@td.mw.tum.de (M. Spinnler), sattelmayer@td.mw.tum.de (T. Sattelmayer)

ABSTRACT

Organic and inorganic fouling continues to be the major limiting factor in membrane processes. It is expected that increasing the wall shear stress by application of pulsating flows will help to reduce fouling and therefore allow treatment of highly polluted water. Furthermore, this can reduce pre-treatment and the quantity of chemicals required, as well as increase the water recovery. This study theoretically and experimentally investigates pulsating flows for mitigation of colloidal fouling in osmotic membrane processes. It is the aim to quantify the potential of pulsating flows to prevent the build-up of a so-called cake layer. An analytic solution in an empty channel, 2-D CFD simulations based on a preliminary study, and experimental results provide insight into the interrelation of Womersley number, amplitude ratio and the hydrodynamic phenomena in pulsating flows. The theoretical investigations show that not only the frequency but also the amplitude ratio has a strong influence on the wall shear stress. The higher the amplitude ratio, the higher the increase in mean wall shear stress relative to the steady-state value. The CFD simulations also indicate that an increasing Womersley number increases the wall shear stress near spacer filaments, which correlates to the area where particles accumulate. The experiments were conducted with a forward osmosis test rig that included a pulsation generator and a corresponding measurement application. A siren was used to reach the high Womersley numbers at which a high increase in wall shear stress was expected. For low frequencies, a solenoid valve was applied. The amplitude ratio was measured based on the differential pressure across an orifice. Experiments showed that the fouling propensity of the process is frequency and amplitude dependent. It could be shown that pulsating flows can mitigate colloidal fouling and therefore increase the permeate flux by up to 20% compared with operation without pulsations.

Keywords: Pulsating flow; Colloids; Fouling; Experiment; Forward osmosis

1. Introduction

Fresh water is a rare resource on our planet. Especially in arid regions, alternative ways to produce and reclaim fresh water are important and in high demand. In the last decades, after a slow start, membrane processes have become increasingly popular. In most membrane processes, pressure is the driving force for separating a feed solution into a permeate and a brine stream. The process preferred for a specific task mainly depends on the given feed water characteristics and necessary permeate quality.

The most common process in desalination is reverse osmosis (RO). Hydraulic pressure is applied to overcome the osmotic pressure difference between a salty feed water and the pure permeate, which are separated by a dense membrane. The related forward osmosis (FO) process can be operated without significant pressure difference. Here, the driving force is an osmotic pressure gradient over the membrane. A so-called draw solution with a high osmotic pressure extracts water from a feed solution. The diluted

---

* Corresponding author.

draw solution must be regenerated to establish a desalination process. This investigation focuses on the first part of the process: the osmotic dilution. The motivation to study osmotic dilution is two-fold. FO is applied for highly contaminated feed waters [1]. It also serves as a model process for RO, but without the need for high pressures. This simplifies the experiments, especially the generation and measurement of pulsating flows.

There are several factors that affect the performance of membrane separation processes: membrane properties, feed water pH, concentration polarization (CP), scaling, and fouling. Today, fouling is the main problem affecting membrane processes and the limiting factor in many applications. It can be separated into organic, biological [2,3], and colloidal [4,5] fouling as well as scaling. Particles in the size range of 1 nm – 1 μm are generally referred to as colloidal particles. They move through the module, agglomerate, and stick to the spacer or the membrane surface. Colloids on the membrane surface participate in forming a cake layer. By blocking the membrane surface this leads to a decrease in the water flux, which results in a decrease in the process efficiency. Particle agglomeration that leads to a blocking of the feed channel and therefore an increase in hydraulic pressure drop over the module presents another mechanism that reduces the process efficiency.

The forces acting on colloidal particles close to the membrane are manifold (Fig. 1). They can be separated into electrostatic interactions (Van der Waals attraction, charge repulsion), forces caused by hydraulic conditions (inertial lift, axial drag, shear induced diffusion), and gravitational forces (sedimentation). The permeation drag is caused by the flux through the membrane. This results in a higher concentration of particles near the membrane surface than in the bulk flow, which leads to a concentration gradient [6].

Chaumeil and Crapper [7] studied the initial deposition of colloidal particles around non-woven membrane spacers. They used the discrete element method in combination with CFD to study colloidal particles in a fluid. They observed that initial deposition patterns typically appear in regions with low wall shear stress and that particles accumulate around filament junctions.

There are several ways to mitigate or slow down the process of cake layer formation. Either the solution is pre-filtered, the feed water pH value is modified, or the hydrodynamic properties are changed, so that the shear stress at the membrane surface is higher. The wall shear stress at the membrane can be increased by increasing the velocity of the feed flow, which also increases the pressure loss over the module, by changing the spacer geometry or by using unsteady operation mechanisms. This paper focuses on the latter approach, unsteady operation mechanisms.

Several approaches for achieving unsteady operation conditions in membrane processes were discussed in literature, including back-pulsing [8], gas sparging [9,10], the vibratory shear enhanced process (VSEP) [11,12], reverse brine flow [13,14], and pulsations [15,16].

Bertram et al. [17] studied the effect of pulsating flows on fouling of silica particles in micro- and ultrafiltration systems and demonstrated a flux enhancement of 60%. Jaffrin et al. [18] studied plasma filtration and demonstrated an enhancement of 45%. Recent research also showed that there could be a significant benefit in operating membrane processes under unsteady conditions to reduce fouling [19,20].

Boo et al. [15] observed a positive effect of a pulsating feed flow on fouling. Nevertheless, the flow was not characterized in respect of the amplitude and frequency of the pulsation. Jalilvand et al. [21] numerically studied the wall shear stress increase caused by pulsating flows in an empty channel and concluded that this increase will also lead to a decrease in fouling. There was neither a quantitative numerical nor experimental evaluation of the influence of wall shear stress generated by pulsating flows on fouling.

Many research papers numerically [16,22–24] and experimentally [25–28] investigated how a pulsating feed flow affects CP in membrane processes. In summary, they concluded that pulsating feed flows lead to a decrease in CP. This results in an increase in water flux through the membrane. An important factor on the overall system efficiency is the additional energy requirement of unsteady operation strategies. Zamani et al. [29] reviewed several publications about fouling mitigation strategies based on unsteady hydrodynamics. They concluded that the VSEP [11] concept has the highest potential for fouling mitigation but results in the highest specific power requirement. They also stated that not enough data could be found about the shear rates in pulsating flows. Therefore, the mitigation potential of pulsating flows was not analyzed. There is a gap in research concerning the effects of pulsating feed flows on fouling in osmotic processes, especially in spacer-filled channels.

It is the objective of this study to show that pulsating flows can be used to mitigate fouling in membrane processes. Pulsating flows affect the wall shear stress on the membrane, but direct measurement is not technically feasible. To gain information about the influence of frequency and amplitude on the shear rate, an analytic solution of the flow in an empty channel was compared with the wall shear stress calculated by CFD in a channel with eddy-promoters [16]. The fouling mitigation potential was then investigated in an experiment, which compared colloidal fouling in steady-state conditions to four cases with varying frequencies in the range of 0.52 to 11.57 Hz. The positive effect of pulsating feed flows leads to a wider operation range, increased water recovery, and therefore a decrease in brine mass flow.
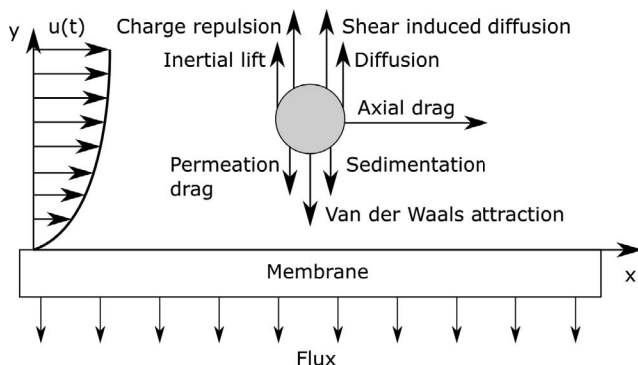

Fig. 1. Forces acting on a colloidal particle near the membrane surface.
Source: Reproduced from reference [6].

2. Characterization of pulsating flows and their influence on wall shear stress

2.1. Parameters characterizing pulsating flows

For usual operation conditions in membrane processes, the flow can be considered as laminar in spiral wound modules [30]. The pulsating flow considered within the scope of this study has a mean Reynolds number below 200 [16]. Although the critical Reynolds number can increase or decrease depending on the transient flow velocity [31], a pulsating flow with a mean Reynolds number below 200 can be considered as laminar. In steady-state, the critical Reynolds number is above 1,000 [32]. Therefore, the following considerations focus only on laminar flows.

The velocity $u(t)$ of the pulsating fluid can be defined as follows:

$$u(t) = \bar{u} + u_{osc}(t) \tag{1}$$

where $\bar{u}$ is the time-averaged velocity and $u_{osc}(t)$ the oscillating component [33]. The time-averaged velocity is given by:

$$\bar{u} = \frac{1}{t_{osc}} \int_0^{t_{osc}} u(t)\,dt \tag{2}$$

Here, t_{osc} is the time interval for one oscillation. The oscillating velocity $u_{osc}(t)$ is defined as the product of the oscillation amplitude $u_{osc,max}$ and a function $f(\omega,t)$, which represents the shape of the transient velocity:

$$u_{osc} = u_{osc,max} f(\omega,t) \tag{3}$$

$f(\omega,t)$ lies between between –1 and 1. The amplitude ratio AR relates $u_{osc,max}$ to $\bar{u}$ [16]:

$$AR = \frac{u_{osc,max}}{\bar{u}} \tag{4}$$

This leads to the following equation for the transient velocity:

$$u(t) = \bar{u}\left(1 + AR\,f(\omega,t)\right) \tag{5}$$

The Womersley number (Wo) is an important dimensionless number in pulsating flows and is, therefore, frequently used to describe blood vessel flows. If Wo < 1, the flow tracks the oscillating pressure gradient and the velocity profile has a parabolic shape. For Wo > 1, the velocity profile is no longer parabolic and there is a phase-shift in time relative to the oscillating pressure gradient [34]. Wo is defined as the ratio between dynamic viscous and convective forces:

$$Wo = \sqrt{\frac{L^2\,\omega}{v}} = \sqrt{2\pi\,Re\,Str} \tag{6}$$

where L is the characteristic length of the channel, which corresponds to the height of the channel, or the diameter of the orifice. Re is the Reynolds number:

$$Re = \frac{L\,u(t)}{v} \tag{7}$$

The Strouhal number Str is defined as follows:

$$Str = \frac{\omega\,L}{2\pi\,u(t)} \tag{8}$$

By inserting Eqs. (3)–(5) into Eq. (1), $u(t)$ can be expressed as follows:

$$u(t) = \bar{u}\left(1 + AR\,f\left(\frac{Wo^2\,v}{L^2}, t\right)\right) \tag{9}$$

2.2. Wall shear stress in empty and spacer-filled channels

The wall shear stress plays a crucial role in fouling and its mitigation [11,35]. A study of the literature reveals that a dynamic shear stress profile can mitigate fouling and increase the performance of heat or mass transfer systems [36].

For the interpretation of the experimental results and to understand the influence of amplitude and frequency on the wall shear stress, the underlying mechanisms of pulsating flows in spacer-filled channels must be investigated. This section gives insight into the interrelation between frequency, amplitude, and the resulting mean wall shear stress from a theoretical point of view. For this purpose, an analytical solution of the Navier–Stokes equations for transient fully developed laminar flows of incompressible Newtonian fluids in an empty channel by Haddad et al. [37] was implemented. This was compared with CFD results based on a preliminary study [16].

Mechanisms appearing in the flow field of spacer-filled channels can be covered in the simplified 2-D geometries of a zig-zag, a cavity, and a submerged spacer. This approach, which is frequently used in literature [16], significantly reduces computational effort in comparison with computing the complex 3-D flow field.

The analytical solution does not consider permeate flow normal to the wall. The permeate flow perpendicular to the main flow direction can be neglected to calculate the wall shear stress, because it is several magnitudes smaller than the main flow velocity. A flux of 30 L m^{-2} h^{-1} equals a permeate velocity of 8.3 · 10^{-6} m s^{-1}. The mean cross-flow velocity chosen in the CFD calculation [16] was 0.11 m s^{-1}. In a short channel, where it can be assumed that the volume flow rate is not reduced significantly by the permeate flow, the permeate flow can be neglected to calculate the wall shear stress. The main difference of CFD and analytical solution is the geometry. The resulting difference will be covered in this section.

Haddad et al. [37] solved the Navier–Stokes equations for transient fully developed laminar flows of incompressible Newtonian fluids in an empty channel:

$$\frac{\partial u}{\partial t} = -\frac{1}{\rho}\frac{\partial p}{\partial x} + v\frac{\partial^2 u}{\partial r^2} \tag{10}$$

where r is the distance from the center of the channel and x is the position in the direction of the mean flow. The fluid must comply with the continuity equations:

$$\frac{\partial u}{\partial x} = 0 \tag{11}$$

and

$$\frac{1}{\rho}\frac{\partial p}{\partial r} = 0 \tag{12}$$

Assuming a sinusoidal pressure gradient, the dimensionless wall shear stress can be calculated as [37] follows:

$$\tau_W = 1 + \tau_{W,\mathrm{osc}}\sin\left(\omega t + \Delta\Theta_\tau\right) \tag{13}$$

with the oscillating component $\tau_{W,\mathrm{osc}}$:

$$\tau_{W,\mathrm{osc}} = \dot{m}_{\mathrm{osc,max}}\frac{\left|\psi_s\left(Wo\right)\right|}{\left|\psi_m\left(Wo\right)\right|} \tag{14}$$

Here, $\dot{m}_{\mathrm{osc,max}}$ is defined as the amplitude of the mass flow rate. The phase shift $\Delta\theta_\tau$ can be calculated as follows:

$$\Delta\Theta_\tau = \tan^{-1}\left(\frac{\Re\left(\psi_s\left(Wo\right)\right)}{\Im\left(\psi_s\left(Wo\right)\right)}\right) + \tan^{-1}\left(\frac{\Re\left(\psi_m\left(Wo\right)\right)}{\Im\left(\psi_m\left(Wo\right)\right)}\right) \tag{15}$$

$\psi_s(Wo)$ is defined as follows:

$$\psi_s\left(Wo\right) = -\frac{2}{Wo\sqrt{i}}\left[\frac{J_{\frac{1}{2}}\left(\frac{i^{3/2}Wo}{2}\right)}{J_{-\frac{1}{2}}\left(\frac{i^{3/2}Wo}{2}\right)}\right] \tag{16}$$

where $J_v(x)$ is the Bessel function for x of the order v. $\psi_m(Wo)$ can be calculated as follows:

$$\psi_m\left(Wo\right) = -\frac{12}{Wo^2}\left[\frac{\sqrt{i}J_{\frac{1}{2}}\left(\frac{i^{3/2}Wo}{2}\right)}{\frac{Wo}{2}J_{-\frac{1}{2}}\left(\frac{i^{3/2}Wo}{2}\right)} + 1\right] \tag{17}$$

This solution was used to calculate the transient wall shear stress τ_w in an empty channel and gives qualitative information on the correlation between Wo, AR, and τ_W for sinusoidal pulsations. It assumes that the shape of the pulsation velocity in the experimental test rig is similar to the sinusoidal pulsation velocity due to inertia effects. Other types of pulsation must be investigated in further studies.

The analytical solution is now compared with the CFD solution [16] of the flow in a channel with zig-zag, submerged, and cavity configuration (Fig. 2). The wall shear stress is calculated for the lower surface in each case. Fig. 3 shows the comparison of the analytical solution with the CFD solution. The mean wall shear stress relative to the steady-state value:

$$\tau_{W,\mathrm{rel,mean}} = \frac{\tau_{W,\mathrm{puls,mean}}}{\tau_{W,\mathrm{Steady,mean}}} \tag{18}$$
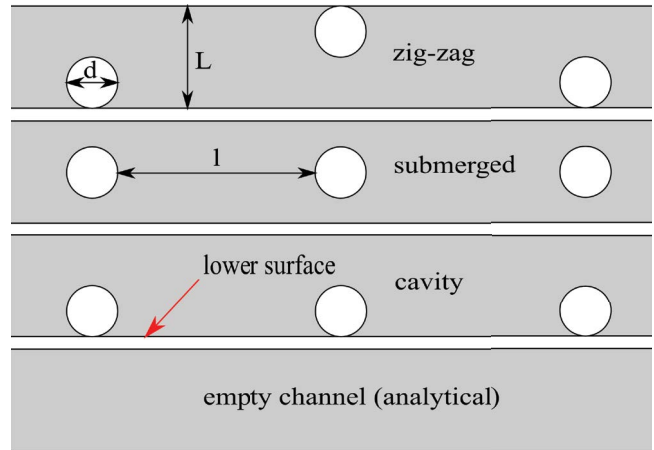

Fig. 2. Visualization of zig-zag, submerged, cavity, and empty channel (analytical solution) configuration of eddy-promoters: $d = 0.5$ mm, $l = 1.5$ mm, and $L = 0.94$ mm. The flow direction is from left to right.

is plotted against the Womersley number. The steady-state values are: 0.236 Pa (zig-zag), 0.722 Pa (submerged), 0.073 Pa (cavity, lower surface), and 0.618 Pa (empty channel, analytical solution). The wall shear stress for the submerged configuration is high in steady-state compared with the other geometries, because the effective cross-section area of the channel is reduced by the spacer. This results in higher velocity gradients at both walls. In the cavity configuration, the free cross-section is reduced as well and the velocity gradient at the upper wall is increased. At the lower membrane the wall shear stress is reduced in the cavity. The latter is shown in Fig. 3. The zig-zag configuration shows regions with low wall shear stress upstream and downstream of the filaments. Nevertheless, an increase in velocity gradient and therefore wall shear stress can be observed in regions where the channel is obstructed by a filament. Therefore, the zig-zag configuration was chosen for further analysis.

The value of $\tau_{W,\mathrm{rel,mean}}$ increases with the Womersley number in both the CFD and analytical solution. It can be seen that pulsating flows have a high impact on the wall shear stress in the cavity configuration. Here, the effect of the changing recirculation zone leads to a significant increase in the velocity gradient at the lower surface [16]. Due to the complex spacer geometry, the zig-zag and submerged configurations have a higher absolute wall shear stress in steady-state than the cavity type. This could be a reason why the enhancement of the relative wall shear stress is lower at a Womersley number of 5.6 for the cavity type. The result for the analytical solution lies between zig-zag and submerged configuration.

Fig. 4 compares the wall shear stress in an empty channel and in a channel filled with eddy promoters [16] for different amplitude ratios. The mean value of the wall shear stress $\tau_{W,\mathrm{rel,mean}}$ increases more with higher AR due to steeper velocity gradients. Other factors play a crucial role for pulsating flows in empty channels or pipes. The Richardson effect and flow reversal, which depend on frequency and amplitude ratio [37], can intensify the mean wall shear stress. In spacer-filled channels with high
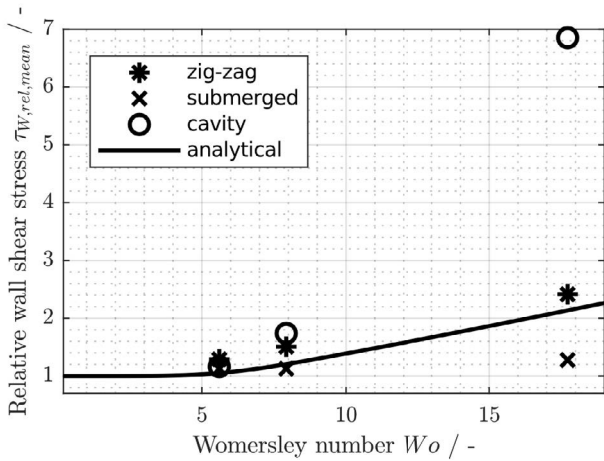
Fig. 3. Relative wall shear stress $\tau_{W,\mathrm{rel,mean}}$ to steady-state values calculated in an empty channel according to the study by Haddad et al. [37]. Comparison with CFD values calculated according to the study by Präbst et al. [16] for zig-zag, cavity, and submerged configuration. All calculations performed for AR = 1. Channel height for both cases: 0.94 mm. Steady-state values: 0.236 Pa (zig-zag), 0.722 Pa (submerged), 0.073 Pa (cavity), and 0.618 Pa (analytical).
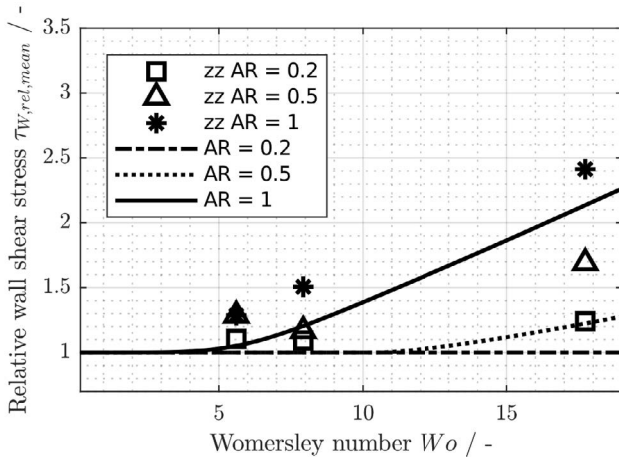

Fig. 4. Comparison of relative wall shear stress for different values of AR. The analytical solution (lines) and CFD solution (discrete points) for the zig-zag (zz) configuration is displayed. Wall shear stress calculated as for Fig. 3.

amplitude ratios, the recirculation zone after the filament changes significantly during one period, whereas at low amplitude ratios only small perturbations occur [16].

In contrast to the effect of pulsating flows in an empty channel, the wall shear stress is a local phenomenon when the channel contains eddy promoters. Fig. 5 shows the relative wall shear stress profile in a channel with zig-zag eddy-promoters for different Womersley numbers at an amplitude ratio of 1 and for different amplitude ratios at a Womersley number of 7.9. An increase in Wo not only leads to a higher value of $\tau_{W,\mathrm{rel,mean}}$ but also a decrease in the distance d_{ab}. d_{ab} is identified in the CFD results as the distance between upstream spacer filament and the point of sign change
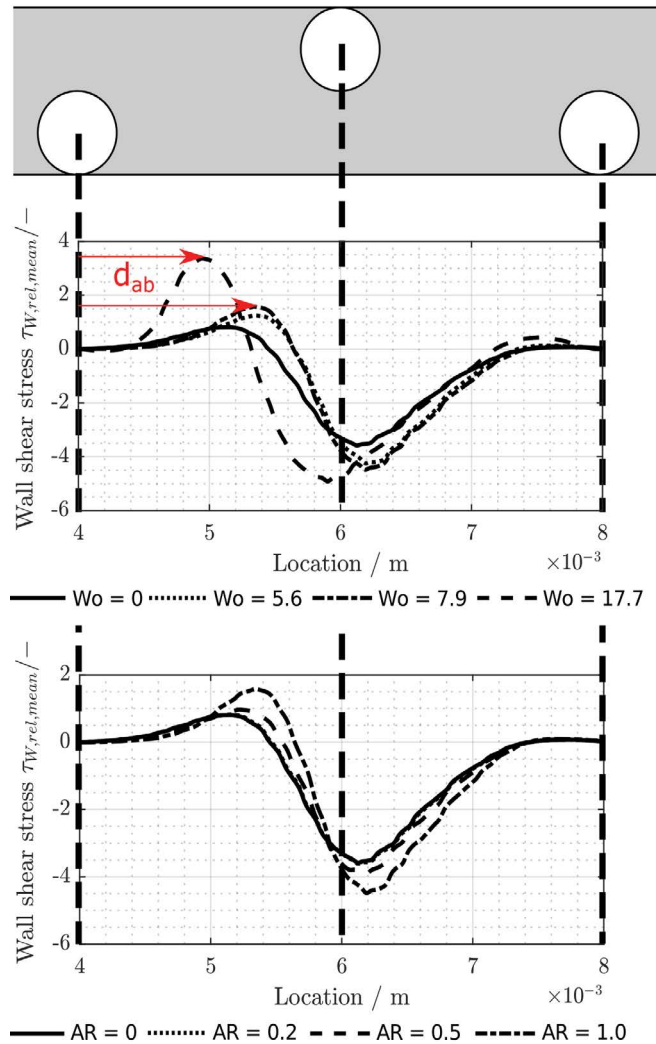

Fig. 5. Sketch of channel with zig-zag eddy promoters and CFD calculation of time-averaged relative wall shear stress at the lower wall. Comparison of several Wo numbers at an AR of 1 and comparison of several ARs at a Wo number of 7.9. d_{ab} indicates the distance from the location of the maximum of the wall shear stress to the eddy-promoter filament.

of the derivative of the wall shear stress. It can be seen in Fig. 5 that the distance d_{ab} is a function of the Womersley number. The higher the Womersley number, the closer the attachment point of the flow to the upstream spacer filament. This leads to a frequency dependent decrease in recirculation zone downstream of the spacer filament and therefore a decrease in d_{ab}. Chaumeil and Crapper [7] stated that areas with low wall shear stress are more likely to be affected by colloidal fouling. In the example of the zig-zag configuration that would be downstream of a spacer filament. Therefore, by decreasing the distance d_{ab} which leads to an increase in time averaged wall shear stress $\tau_{w,\mathrm{rel,mean}}$, the area where particles are likely to deposit is reduced. An increase in amplitude ratio changes the maximum value as well as the size of the time-averaged recirculation zone. The changing size of the recirculation zone is indicated by the changing position of the zero-crossing points.

3. Experimental methods

3.1. Bench-scale forward osmosis fouling experiment

The experiments were conducted with the set-up shown in Fig. 6. The cross-flow cell was custom built. The dimensions of the channels on both sides of the membrane were 11.5 cm by 10 cm by 0.86 mm. The membrane area was 115 cm^2. A diamond-type RO 34 mil AMI feed spacer was used on the feed side and a finer, non-woven spacer on the draw side (Table A1).

In the feed cycle, fluid was pumped from a reservoir through the test cell. Further details on the feed solution's content are presented in Section 3.3. Within the draw cycle, the highly concentrated salt solution was pumped from a second reservoir through the test cell. The draw solution chosen was an aqueous solution of NaCl. At the beginning of the experiment, it contained 150 g kg^{-1} NaCl.

The pressure in the middle of the test cell was held constant at 1.1 ± 0.01 bar by regulating the pump. The volume flow rate through the test cell was held at 40 ± 0.5 L h^{-1} ($u \approx 0.13$ m s^{-1}) by the motorized needle valve NV, which is a compromise between the measurement error of the orifice and fouling due to low velocities. The temperature was 23°C ± 1°C. The experiments were carried out at a pH of 6–7. The masses of the draw and feed solution were measured continuously using scales.

The pulsating flows were generated in two different ways. For slow pulsations in the range of 0.1–4 Hz a solenoid valve was used. The duty value, which defines how long the valve stays open, could be modified to regulate the amplitude. For pulsations in the range 4–20 Hz, a siren (also referred to as rotating distributor disc [38]) was used. In this case, regulation of the pulsation amplitude was not possible. Both pulsation devices generate velocity pulsations
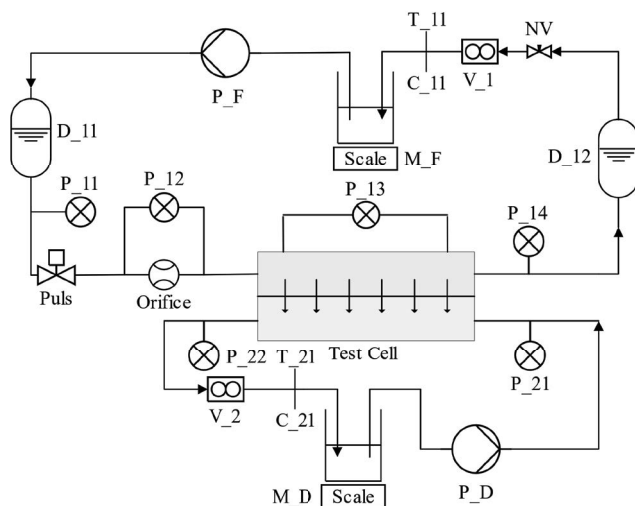
by inducing a transient hydraulic resistance. A stainless-steel pipe connected the pulsation device with the orifice and the test cell to decrease energy losses upstream of the test rig. Pulsation dampers (D_11 and D_12) were necessary upstream of the pulsation generator and downstream of the test cell to limit pulsations outside the measurement and test section and thus avoid damage to the measurement devices or the pump. Similar to the effect of inductors on the voltage in an electrical circuit, pulsation dampers limit the pressure spikes inside a hydraulic circuit. In general, gear pumps were used to generate pulsation free flows. Pulsations produced by the pumps were fully damped by the piping to the test section. Only the pulsations generated by the pulsation devices influenced the feed flow rate.

An orifice (94D-MBL 500D, Dosch Messapparate GmbH, Berlin, Germany) was used to determine the transient mass flow rate $\dot{m}$. A pressure sensor P_12 measured the differential pressure across the orifice. The pressure drop was used to calculate $\dot{m}$ downstream of the pulsation generation device, based on Doblhoff-Dier et al. [39]. They related the pressure drop Δp across an orifice to $\dot{m}$:

$$\Delta p = \frac{A}{\rho}\dot{m}^2 \text{sign}(\dot{m}) + B\frac{d\dot{m}}{dt} \tag{19}$$

where A is an indirect function of the mean mass flow rate $\dot{m}_{\text{mean}}$, and B is assumed as constant. Parameter A depends on fluid properties, flow resistances, as well as the geometry of the aperture and could be derived by measuring Δp at several steady-state mass flow rates $\dot{m}_{\text{mean}}$. B was chosen in dynamic conditions so that the mean value of the mass flow rate calculated by Eq. (19) is the same as $\dot{m}_{\text{mean}}$, which was measured by V_1. The measurement error of this method is directly related to frequency, mean mass flow rate, velocity amplitude, and the signal-to-noise ratio (SNR), especially for pulsating flows with high amplitude ratios and high-pressure wave propagation velocities. Eq. (19) represents a strong simplification, which is not able to represent the complex phenomena of pulsating flows in an orifice. The error made by this assumption cannot be given in the scope of this study. For this reason, a conservative estimation of the error of the AR calculation based on the noise of the measurement signal was derived. The highest deviation was in the range of 30%–40% (Appendix C). Table A2 contains a detailed list of the equipment that was used in the experiment.

3.2. Membrane preparation

A new brackish water RO membrane (TML, Toray membrane, INC., Poway, California, United States) was used for each fouling experiment. The sample was rinsed in deionized (DI) water for 24 h before use. Afterwards, each membrane sample was used in an FO set-up without foulants for at least 12 h to ensure that the process was stable before foulants were introduced. The pressure difference between feed and draw was 0.8 bar and the pH 6–7.

3.3. Colloidal fouling experiments

Silica particles (silica, fumed, Sigma-Aldrich, St. Louis, Missouri, United States) with a diameter of 0.2–0.3 μm were

Fig. 6. Piping and instrumentation diagram of the test rig. D: pulsation dampers; Orifice: device to measure amplitude and frequency of pulsation; NV_1: automated needle valve to regulate volume flow; Puls: pulsation generation device, either valve or siren; Module: FO test cell; T_*: temperature sensors; C_*: salinity sensors, P_F and P_D: pumps; P_*: pressure sensors; M_*: scale; V_*: volume flow sensors.

used as model foulants. Suspensions at the desired concentration were prepared by dispersing the silica powder in DI water. Prior to use, the samples were stirred for at least 30 min to ensure complete dispersion.

The feed solution, with a mass of 3,800 g, was prepared with a colloid concentration of 4 g L^{-1}. After the membrane preparation, the fouling experiment was conducted in batch mode. This means that the feed solution was continuously concentrated over the course of the fouling experiment (Fig. 9). The experiment was stopped when the colloidal concentration reached 6.1 g L^{-1}.

Fouling can be characterized by a normalized flux as follows:

$$j_{N0} = \frac{j_F}{j_0} \tag{20}$$

which is the ratio of the flux during the fouling experiment j_F to the flux at the start of the fouling experiment j_0.

The diffusion of water from feed to draw cycle causes a dilution of the draw solution. The driving force for diffusion therefore decreases. A baseline test (Fig. 8) was carried out to account for dilution of draw solution and salt concentration in the feed solution. This baseline experiment was conducted to generate a factor $j_{dil,N}$, that could be used to account for dilution in the normalized factor j_N. A linear fit over the normalized flux was then used to calculate $j_{dil,N}$.

$$j_N = \frac{j_F}{j_0 \, j_{dil,N}} \tag{21}$$

The normalized flux j_N accounts for dilution and concentration of draw and feed. Therefore, a decrease in flux was caused by colloidal fouling.

4. Results

4.1. Pulsation parameters

Fig. 7 shows the AR plotted against the Wo number and frequency at the start of the fouling experiment. The pulsating flow was generated either by a valve (0.52 and 2.65 Hz) or by the siren (6.57 and 11.57 Hz). The transient mass flow was measured according to Section 3.1. The frequency of the measured pulsation was used to calculate the Wo number in the channel of the test cell according to Eq. (6). The AR was calculated according to Eq. (4). It can be seen that the pulsation at 6.57 Hz, which was generated by the siren, has the highest amplitude ratio (AR = 1.4). At a frequency of 11.57 Hz, the AR is significantly lower (AR = 0.4). The pulsation that was generated by the valve shows an AR of 0.36 at a frequency of 0.52 Hz and AR = 0.62 at a frequency of 2.65 Hz.

4.2. Baseline experiments

According to Section 3.3, a baseline experiment was conducted to account for the dilution of the draw solution and the back-diffusion of NaCl during a fouling experiment. In the real system, the flux decrease is not a linear function of the osmotic pressure difference due to CP. However, due to the small variation in overall mass (20 L of draw solution to
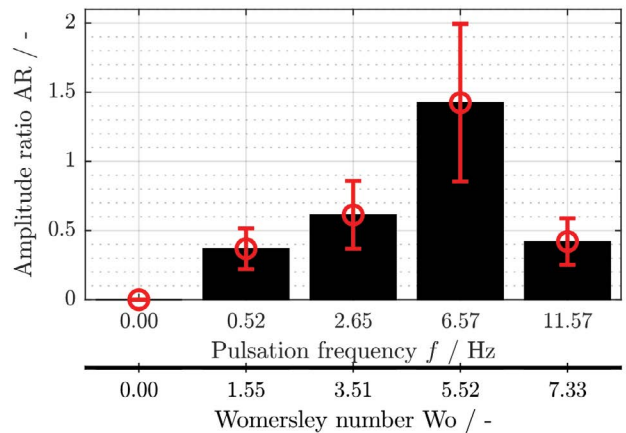

Fig. 7. Amplitude ratio AR plotted against pulsation frequency f and Womersley number Wo. The Wo number was calculated from the frequency. The frequency was calculated by FFT of the differential pressure measured across the orifice (Appendix B). AR was calculated according to Eq. (4). Measurement error (red line) of 40% assumed according to Appendix C.
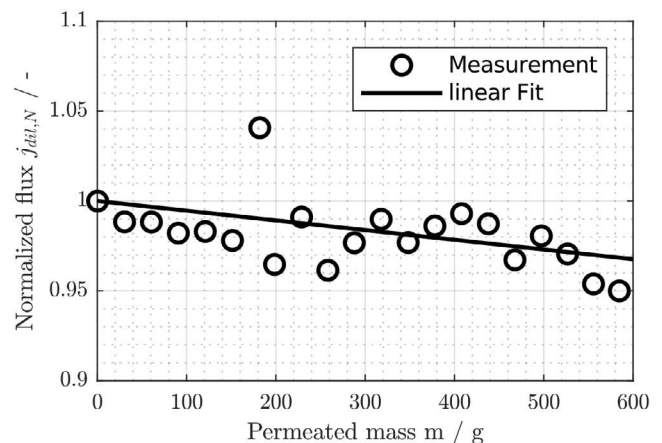

Fig. 8. Baseline experiment. Decrease in osmotic pressure difference $\Delta\pi$ due to back-diffusion of NaCl from draw solution to feed solution and dilution of draw solution. The experiment started at w = 150 g L^{-1} NaCl. The velocities were 0.13 m s^{-1} for the feed, and 0.12 m s^{-1} for the draw. The operating temperature was 23.0°C ± 1.0°C. The mean pressure difference between feed and draw was 0.8 bar. The linear fit was used to normalize the measured fouling experiments with respect to the dilution of the process. The uncertainty propagation of the measurement error of the scales resulted in a maximum error of 3.53% for the flux.

21.3 L at the end of the experiment), the flux shows an almost linear behavior. Therefore, a linear fit was chosen to correct for osmotic dilution. Fig. 8 shows the measured data and the linear fit that is later used to account for osmotic dilution.

4.3. Colloidal fouling experiments

The fouling experiments were conducted in batch mode according to Section 3.3. This means the feed solution is further concentrated during the experiment. Fig. 9 shows the calculated increase in colloid concentration in the feed

system plotted against the water mass that has passed through the membrane. The colloid concentration at the start was 4 g L^{-1} and increased up to 6.1 g L^{-1}.

Fig. 10 shows the normalized flux, calculated according to Section 3.3, plotted against the permeated mass. The different test cases, f = 0, 0.52, 2.65, 6.57, and 11.57 Hz are compared with each other. The highest fouling rate appears for the steady-state case, whereas there is no fouling for f = 11.57 Hz. It can also be seen that a higher frequency leads to less fouling. Both observations are related to the increase in wall shear stress caused by a higher Womersley number (Fig. 5).
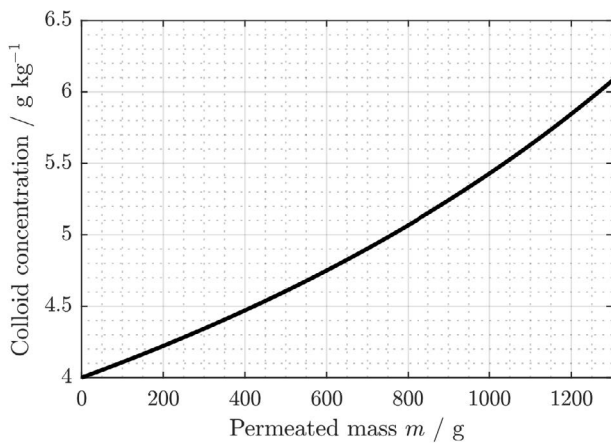

Fig. 9. Colloid concentration against permeated mass. The concentration increases as the mass of the feed solution decreases. The initial mass of feed solution was 3,800 g.
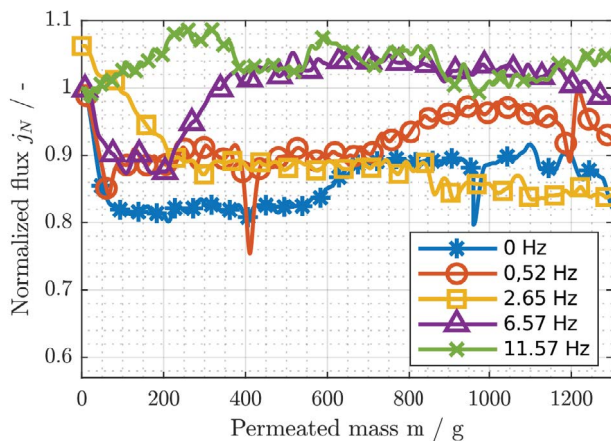

Fig. 10. Normalized flux plotted against the permeated water mass. The decrease in the osmotic pressure difference $\Delta\pi$ due to back-diffusion of NaCl from draw solution to feed solution and dilution of draw solution was accounted for in the normalized flux by the baseline experiments. Fouling runs were performed at pH 6–7. Initially, the draw solution contained 150 g L^{-1} NaCl and the feed solution 4 g L^{-1} colloids. The velocities were 0.13 m s^{-1} for the feed, and 0.12 m s^{-1} for the draw. The operating temperature was 23.0°C ± 1.0°C. The mean pressure difference between feed and draw was 0.8 bar. The uncertainty propagation of the measurement error of the scales resulted in a maximum error of 3.53% for the flux.

A closer look at the results of Fig. 10 reveals two phenomena. First, the initial slope of the flux differs for each experiment after the injection of particles. The initial flux decline depends on the frequency and the amplitude ratio, since an increase in frequency and amplitude ratio leads to an enhancement in mixing. This enhancement in mixing may lead to a faster initial agglomeration of particles on the membrane surface due to a better distribution of particles in the module. The second phenomenon, which was sometimes observed, is jumps in the flux profile after the build-up of a cake layer. This phenomenon could be observed for the steady-state case at a permeate mass of 600 g, for f = 0.52 Hz between a permeate mass of 600 and 800 g, and for f = 6.57 Hz at a permeate mass of 400 g. This could be the point where the cake layer is partially removed, because the shear force is higher than the adhesion force. Both effects are expected to provide significant statistical scatter. Therefore, a general deduction cannot be drawn. In the case of f = 11.57 and 6.57 Hz, the normalized flow reaches a value which is higher than unity. This could be caused either by not choosing the right starting point (Section 3.3) of the flux before the fouling experiment or by the osmotic dilution correction (Section 4.2).

Fig. 11 shows the pressure difference Δp over the feed channel as function of discrete values of permeated water mass. The graph displays the different frequencies 0.52, 2.56, 6.57, and 11.57 Hz. It can be seen that Δp remains almost constant for 11.57 Hz, while it changes significantly for 0.52, 2.65, and 6.57 Hz. This is caused by the change in hydraulic pressure resistance inside the test cell that accompanies fouling. The maximum and minimum values are important parameters to consider, as they give an indication of the transient velocity inside the test cell. Negative values for the minimum mean that there is a negative mean flow direction within one pulsation period. The fluctuation for f = 11.57 Hz is the lowest.

Fig. 12 shows a statistical evaluation of the normalized flux for each fouling experiment. It indicates that the median of the normalized flux increases with Wo. At the highest Wo (Wo = 7.33), the scatter is very limited, whereas the flux differs significantly in the case of Wo = 1.55. The median for the highest Wo is 24% higher than the median for the
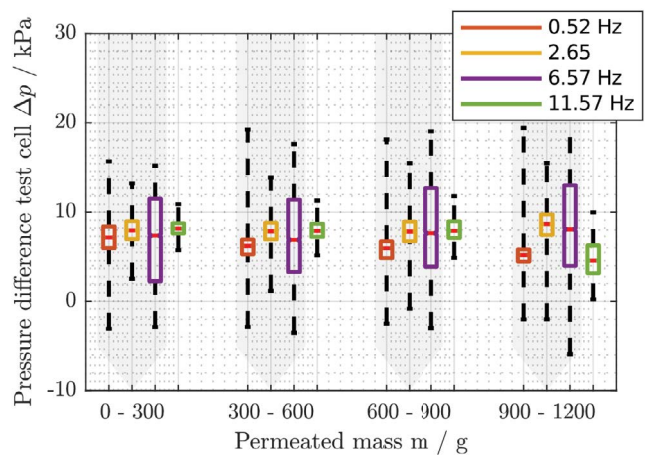

Fig. 11. Statistical evaluation of the differential pressure across the test cell. Evaluation for each permeated mass range.
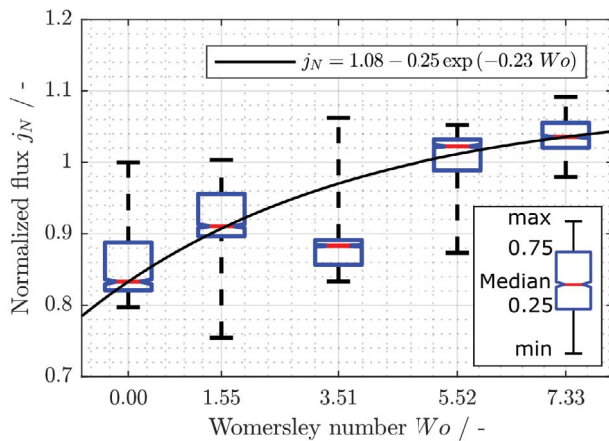
Fig. 12. Statistical evaluation of normalized flux plotted against Wo number. It contains the whole fouling run from insertion of particles until reaching the final particle concentration. Whiskers of the boxplot are defined so that they cover all outliers. Boxplot boundaries are the 0.25 and 0.75 quantiles, respectively. The line in the middle of each boxplot corresponds to the median of the underlying data. Operating parameters according to Fig. 10.

steady-state case. The flux values indicated by the median were used for an exponential fit.

5. Discussion

5.1. Influence of Womersley number on fouling mitigation

A quantitative analysis of the Womersley number's fouling mitigation potential is difficult due to the different amplitude ratios in each conducted experiment. Nevertheless, a qualitative result can be obtained: Pulsating flows have the potential to suppress or decrease colloidal fouling, which agrees with the findings of Boo et al. [15].

The CFD results (Section 2.2) give an insight into the changes in hydrodynamic forces that are caused by pulsating flows. They indicate that an increase in AR or Wo leads to different wall shear stress profiles, as well as an increase in mean wall shear stress at the membrane surface. It is assumed that the wall shear stress is the main variable to affect colloidal fouling that can be influenced by periodic hydrodynamic perturbations. Other forces that act on colloidal particles (Fig. 1), which might be influenced by AR or Wo, cannot be analyzed separately.

The experimental results show a qualitative trend between Womersley number and fouling mitigation (Fig. 12). This tendency seems to follow an exponential equation:

$$j_N(Wo) = a + \exp(-k\,Wo) \tag{22}$$

where k defines the effect of pulsating flows on fouling. It is expected to be dependent on several factors, including colloidal concentration, flux, and amplitude ratio. The constant b is defined by the steady-state fouling experiment. This factor depends on the same principal mechanisms that concerns fouling in membrane processes. The factor a defines the asymptote at Wo → ∞. The factor a reaches a value higher

than unity, because the normalized flux of the experiment with a Womersley number of 7.33 reaches higher than 1 (Section 4.3).

To our knowledge, there has not yet been a quantitative analysis of colloidal fouling mitigation by pulsating flows. Therefore, the pulsating component of the model cannot be validated by literature values. This is not the case for the steady-state experiment, which is comparable with several FO papers. One of them, Lee et al. [40], studied the difference of RO and FO. They used 400 mg L^{-1} of colloidal suspension with 300 nm silica colloids and had an initial flux of 5.23 μm s^{-1} (18.72 L m^{-2} h^{-1}) and ended at 3 μm s^{-1} (10.8 L m^{-2} h^{-1}) after 15 h. This corresponds to a decrease of 42.3%. The amount of flux decrease due to colloidal fouling is a lot higher than the amount seen in this study. That was expected, as the initial flux is a lot lower in this study 6 L m^{-2} h^{-1}, which leads to less permeation drag that affects the particles. Therefore, the cake layer is less stable in this study.

It can be seen in Fig. 10 that the cake layer is not stable. The flux increases in steady-state conditions and at frequencies 0.52 and 6.57 Hz after a certain mass has passed the membrane. During the fouling process, the cake layer grows laterally as well as in thickness until a certain point. This point is reached when the hydraulic forces are finally high enough to cancel out the permeation drag and adhesion forces, which causes the cake layer to debond. The lower flux compared with other FO studies is attributable to the RO membrane and the high internal CP. RO membranes were used because they provide higher stability and therefore decrease the vibration amplitude of the membrane surface. These vibrations distort the interpretation of the experimental results. The internal CP cannot be directly calculated from the data gained in the experiment. However, a comparison can be drawn between the osmotic pressure difference between draw and feed solution and the osmotic pressure difference seen in the resulting flux. Given the draw solution's parameters of the steady-state experiment without any colloids (u = 0.12 m s^{-1}, T = 23°C, w = 150 g kg^{-1} NaCl) one can calculate the osmotic pressure difference as 146.2 bar. The real osmotic pressure difference that results in a flux of 6 L m^{-2} h^{-1} is 14.7 bar. This difference of 131.5 bar is a result of the internal CP, CP by back-diffusion into the feed solution, and CP on the draw side. When colloids deposit on the membrane, the effect of cake-enhanced osmotic pressure further adds to this.

5.2. Influence of wall shear stress on fouling mitigation

The comparison of the analytic and CFD calculations has demonstrated that the wall shear stress correlates with both AR (Fig. 4) and Womersley number (Fig. 3). An increase in AR, as well as Wo leads to an increase in wall shear stress. The main effect of the wall shear stress is to prevent particles from accumulating on the membrane surface. Therefore, it can be expected that an increase in AR and Wo leads to a decrease in particle accumulation on the membrane surface and therefore a decrease in fouling propensity of the system.

At a Wo number of 7.9 and an AR between 0.2 and 0.5, the difference in wall shear stress between pulsating flow

and steady-state case lies between 5% and 10% for the zig-zag configuration (Fig. 4). Although the CFD simulations just investigated simplified 2-D geometries, a similar trend is visible in Fig. 12. The median flux at steady-state ($j_N = 0.84$) was 20% lower in comparison with pulsating ($j_N = 1.04$) conditions at a Wo number of 7.33.

The CFD calculation of the wall shear stress in combination with the assumption that the wall shear stress is solely responsible for fouling mitigation would underestimate the fouling mitigation potential of pulsating flows. This could either be explained by the various mechanisms that influence the build-up of a cake layer (Section 1), or the vibrations caused by the different pressure fluctuations of feed and draw channel. This might also have an impact on fouling mitigation and is certainly dependent on the pulsation frequency. By application of a defined pressure difference across the membrane and by using a fine spacer in the draw channel, vibrations were suppressed to a minimum.

For a complete comparison between simulations and experimental results a detailed model must be developed. Nevertheless, the simplified 2-D calculations already help to predict mechanisms involved in particle accumulation under pulsating flow conditions.

5.3. Influence of amplitude ratio on fouling mitigation

The effect of an increase in Wo number and AR is two-fold, Section 2.2: It increases the mean value of the wall shear stress and decreases the distance of the maximum wall shear stress to the upstream eddy promoters. This leads to a smaller recirculation zone where particles are prone to accumulate. The effect of both parameters on fouling mitigation can be seen in Fig. 12. The flux enhancement is comparable in the case of Wo = 7.33 ($j_N = 1.04$) and Wo = 5.52 ($j_N = 1.02$). While the Womersley number is lower in the second case, the amplitude ratio is higher (AR = 1.4 vs. AR = 0.4). This indicates that an increase in AR influences the wall shear stress and therefore the fouling behavior in a similar way to the Wo number.

The amplitude ratio displayed in Fig. 7 must be considered with care (Appendix C). The lower the SNR of the measured pressure signal, the higher the error. It could also be observed that it becomes more difficult to interpret the pressure signal with a higher frequency. It can be seen in Fig. 5 that a change in amplitude ratio leads to an increase in mean wall shear stress, but the localized wall shear stress near the upstream eddy promoter does not change much in comparison with its response to a change in Womersley number. Because fouling would appear in areas with low wall shear stress, the influence of the cumulative measurement error on fouling can be estimated as small.

6. Conclusion

The effect of pulsating flows on colloidal fouling has been evaluated. A novel test rig for pulsating feed flows in FO has been presented that incorporates amplitude measurement and two pulsation generation devices. The experiments cover a broad range of frequencies, 0.52 to 11.57 Hz, and amplitude ratios between 0.35 and 1.4.

In conclusion, pulsations mitigate or reduce fouling. The wall shear stress was identified as the most important parameter that can be influenced by pulsating flows and helps to reduce fouling. It depends on both the Womersley number and amplitude ratio. In the fouling experiment with pulsations, less flux decline caused by colloidal fouling was observed. The trends observed in the experimental results could be explained by effects identified in 2-D CFD results for Womersley numbers below 8.

Pulsations are also expected to improve other membrane processes and reduce fouling phenomena that are significantly influenced by a higher wall shear stress. To better understand the correlation between pulsating flows and fouling mitigation, which is imperative to forecast the fouling mitigation potential of any membrane process, more experiments must be conducted that investigate the effects of amplitude ratio and Womersley number separately at lab-scale. With these lab-scale measurements, the fouling mitigation potential could also be forecast for spiral wound modules, where the amplitude ratio of the pulsating flow changes over the length of the module due to damping effects.

Symbols

Abbreviations

CP	—	Concentration polarization
DI	—	Deionized
FO	—	Forward osmosis
RO	—	Reverse osmosis
SNR	—	Signal-to-noise ratio
VSEP	—	Vibratory shear enhanced process

Variables

Θ_τ	—	Phase shift
v	—	Kinematic viscosity, $m^2\ s^{-1}$
$\Delta\pi$	—	Osmotic pressure difference, Pa
ρ	—	Density, $kg\ m^{-3}$
τ	—	Wall shear stress, Pa
$\tau_{W,rel,mean}$	—	Wall shear stress relative to steady-state
ψ_m	—	Term used to calculate the pressure gradient
ψ_s	—	Term used to calculate the wall shear stress
ω	—	Angular frequency, s^{-1}
AR	—	Amplitude ratio
d	—	Distance, m
f	—	Frequency, Hz
j	—	Mass flux, $L\ m^{-2}\ h^{-1}$
J_v	—	Bessel function of order v
L	—	Characteristic length, m
$\dot{m}$	—	Mass flow, $kg\ s^{-1}$
p	—	Pressure, Pa
r	—	Radius, m
Re	—	Reynolds number
Str	—	Strouhal number
t	—	Time, s
u	—	Velocity, $m\ s^{-1}$
$\bar{u}$	—	Time-averaged velocity, $m\ s^{-1}$
w	—	Mass fraction, $g\ kg^{-1}$
Wo	—	Womersley number
x	—	Position, m

Indices

0	—	Start
dil	—	Diluted
F	—	Fouling
max	—	Maximum value
mean	—	Mean value
N	—	Normalized
Puls	—	Pulsating
osc	—	Oscillating
Steady	—	Steady-state
W	—	Wall

References

[1] K. Lutchmiah, A.R.D. Verliefde, K. Roest, L.C. Rietveld, E.R. Cornelissen, Forward osmosis for application in wastewater treatment: a review, Water Res., 58 (2014) 179–197.

[2] J.S. Baker, L.Y. Dudley, Biofouling in membrane systems — a review, Desalination, 118 (1998) 81–89.

[3] S.E. Kwan, E. Bar-Zeev, M. Elimelech, Biofouling in forward osmosis and reverse osmosis: measurements and mechanisms, J. Membr. Sci., 493 (2015) 703–708.

[4] Y. Yoon, R.M. Lueptow, Concentration of colloidal silica suspensions using fluorescence spectroscopy, Colloids Surf., A, 277 (2006) 107–110.

[5] C.Y. Tang, T.H. Chong, A.G. Fane, Colloidal interactions and fouling of NF and RO membranes: a review, Adv. Colloid Interface Sci., 164 (2011) 126–143.

[6] S.H. Yoon, C.H. Lee, K.J. Kim, A.G. Fane, Three-dimensional simulation of the deposition of multi-dispersed charged particles and prediction of resulting flux during cross-flow microfiltration, J. Membr. Sci., 161 (1999) 7–20.

[7] F. Chaumeil, M. Crapper, DEM simulations of initial deposition of colloidal particles around non-woven membrane spacers, J. Membr. Sci., 442 (2013) 254–263.

[8] E. Brito-de la Fuente, B. Torrestiana-Sánchez, E. Martínez-González, J.M. Mainou-Sierra, Microfiltration of whole milk with silicon microsieves: effect of process variables, Chem. Eng. Res. Des., 88 (2010) 653–660.

[9] C. Cabassud, S. Laborie, L. Durand-Bourlier, J.M. Lainé, Air sparging in ultrafiltration hollow fibers: relationship between flux enhancement, cake characteristics and hydrodynamic parameters, J. Membr. Sci., 181 (2001) 57–69.

[10] Z.F. Cui, S. Chang, A.G. Fane, The use of gas bubbling to enhance membrane processes, J. Membr. Sci., 221 (2003) 1–35.

[11] W. Shi, M.M. Benjamin, Effect of shear rate on fouling in a Vibratory Shear Enhanced Processing (VSEP) RO system, J. Membr. Sci., 366 (2011) 148–157.

[12] A. Subramani, J. DeCarolis, W. Pearce, J.G. Jacangelo, Vibratory shear enhanced process (VSEP) for treating brackish water reverse osmosis concentrate with high silica content, Desalination, 291 (2012) 15–22.

[13] M. Uchymiak, A.R. Bartman, N. Daltrophe, M. Weissman, J. Gilron, P.D. Christofides, W.J. Kaiser, Y. Cohen, Brackish water reverse osmosis (BWRO) operation in feed flow reversal mode using an ex situ scale observation detector (EXSOD), J. Membr. Sci., 341 (2009) 60–66.

[14] X. Lu, E. Kujundzic, G. Mizrahi, J. Wang, K. Cobry, M. Peterson, J. Gilron, A.R. Greenberg, Ultrasonic sensor control of flow reversal in RO desalination-Part 1: mitigation of calcium sulfate scaling, J. Membr. Sci., 419–420 (2012) 20–32.

[15] C. Boo, M. Elimelech, S. Hong, Fouling control in a forward osmosis process integrating seawater desalination and wastewater reclamation, J. Membr. Sci., 444 (2013) 148–156.

[16] A. Präbst, F. Kiefer, A. Kroiß, M. Spinnler, T. Sattelmayer, Influence of dynamic operation of reverse osmosis systems on fluid dynamics and mass transfer by investigation of 2-D spacer filled channels, Desal. Wat. Treat., 73 (2017) 22–26.

[17] C.D. Bertram, M.R. Hooglandb, H. Lib, R.A. Odell, A.G. Faneb, B. Engineering, N. South, Flux enhancement in crossflow microfiltration collapsible-tube pulsation generator, J. Membr. Sci., 84 (1993) 279–292.

[18] M.Y. Jaffrin, L.H. Ding, B.B. Gupta, Rationale of filtration enhancement in membrane plasmapheresis by pulsatile blood flow, Life Support Syst. J. Eur. Soc. Artif. Organs, 5 (1987) 267–271.

[19] Q. Ge, M. Ling, T.S. Chung, Draw solutions for forward osmosis processes: developments, challenges, and prospects for the future, J. Membr. Sci., 442 (2013) 225–237.

[20] A.J. Ansari, F.I. Hai, T. He, W.E. Price, L.D. Nghiem, Physical cleaning techniques to control fouling during the pre-concentration of high suspended-solid content solutions for resource recovery by forward osmosis, Desalination, 429 (2018) 134–141.

[21] Z. Jalilvand, F. Zokaee Ashtiani, A. Fouladitajar, H. Rezaei, Computational fluid dynamics modeling and experimental study of continuous and pulsatile flow in flat sheet microfiltration membranes, J. Membr. Sci., 450 (2014) 207–214.

[22] V.I. Baikov, P.K. Znovets, Membrane processes of separation of solutions in a pulsating flow, J. Eng. Phys. Thermophys., 77 (2004) 802–807.

[23] A.P. Reverberi, V.P. Meshalkin, C. Cerrato, Y.O. Savina, Dynamics of a reverse osmosis unit with application to pulsating regimes for process optimization, Theor. Found. Chem. Eng., 45 (2011) 190–197.

[24] A. Emad, A. Ajbar, I. Almutaz, Periodic control of a reverse osmosis desalination process, J. Process Control., 22 (2012) 218–227.

[25] T.J. Kennedy, R.L. Merson, B.J. McCoy, Improving permeation flux by pulsed reverse osmosis, Chem. Eng. Sci., 29 (1974) 1927–1931.

[26] N.M. Al-Bastaki, A. Abbas, Periodic operation of a reverse osmosis water desalination unit, Sep. Sci. Technol., 33 (1998) 2531–2540.

[27] A. Abbas, N. Al-Bastaki, Flux enhancement of RO desalination processes, Desalination, 132 (2000) 21–27.

[28] C. Rodrigues, M. Rodrigues, V. Semiao, V. Geraldes, Enhancement of mass transfer in spacer-filled channels under laminar regime by pulsatile flow, Chem. Eng. Sci., 123 (2015) 536–541.

[29] F. Zamani, J.W. Chew, E. Akhondi, W.B. Krantz, A.G. Fane, Unsteady-state shear strategies to enhance mass-transfer for the implementation of ultrapermeable membranes in reverse osmosis: a review, Desalination, 356 (2015) 328–348.

[30] G.A. Fimbres-Weihs, D.E. Wiley, Review of 3D CFD modeling of flow and mass transfer in narrow spacer-filled channels in membrane modules, Chem. Eng. Process. Process Intensif., 49 (2010) 759–781.

[31] M.Ö. Çarpinlioğlu, E. Özahi, An updated portrait of transition to turbulence in laminar pipe flows with periodic time dependence (a correlation study), Flow Turbul. Combust., 89 (2012) 691–711.

[32] S.M. Mojab, S.B. Beale, J.G. Pharoah, A. Pollard, E.S. Hanff, Reynolds Number Effects on Flow in a Spacer-filled Channel, In 20th Annual Conference of the CFD Society of Canada, Canmore, Alberta, 2012, doi:10.1006/adnd.1995.1002.

[33] C. Boxler, W. Augustin, S. Scholl, Composition of milk fouling deposits in a plate heat exchanger under pulsed flow conditions, J. Food Eng., 121 (2014) 1–8.

[34] C. Loudon, A. Tordesillas, The use of the dimensionless Womersley number to characterize the unsteady nature of internal flow, J. Theor. Biol., 191 (1998) 63–78.

[35] M. Frappart, M.Y. Jaffrin, L.H. Ding, V. Espina, Effect of vibration frequency and membrane shear rate on nanofiltration of diluted milk, using a vibratory dynamic filtration system, Sep. Purif. Technol., 62 (2008) 212–221.

[36] M. Förster, W. Augustin, M. Bohnet, Influence of the adhesion force crystal/heat exchanger surface on fouling mitigation, Chem. Eng. Process. Process Intensif., 38 (1999) 449–461.

[37] K. Haddad, Ö. Ertunç, M. Mishra, A. Delgado, Pulsating laminar fully developed channel and pipe flows, Phys. Rev. E - Stat. Nonlin. Soft Matter Phys., 81 (2010) 1–13.

[38] E. Spiazzi, J. Lenoir, A. Grangeon, A new generator of unsteady-state flow regime in tubular membranes as an anti-fouling technique: a hydrodynamic approach, J. Membr. Sci., 80 (1993) 49–57.

[39] K. Doblhoff-Dier, K. Kudlaty, M. Wiesinger, M. Gröschl, Time resolved measurement of pulsating flow using orifices, Flow Meas. Instrum., 22 (2011) 97–103.

[40] S. Lee, C. Boo, M. Elimelech, S. Hong, Comparison of fouling behavior in forward osmosis (FO) and reverse osmosis (RO), J. Membr. Sci., 365 (2010) 34–39.

Appendix A. Bench-scale test rig experiments

Table A1
Test cell

Description	Specification
Membrane	
Type	Cross-linked fully aromatic polyamide composite
Vendor	Toray Membrane, INC., Poway, United States
Product type	TML10D
Test conditions	
Feed water pressure	15.5 bar
Feed water temperature	25°C
Feed water concentration	2 g L⁻¹ NaCl
Recovery rate	15%
Feed water pH	7
Test result	
Minimum salt rejection	99.65%
Minimum product flux	33.56 L m⁻² h⁻¹
Feed spacer	
Vendor	AMI, Applied Membranes, Inc., Vista, United States
Product type	M-T4040ALE Feed Spacer
Mesh size	4 mm
Filament diameter	0.25 mm
Hydrodynamic angle	45°
Filament angle AMI	90°
Draw spacer	
Vendor	DelStar Technologies, Inc., Middletown, CT, United States
Product type	N01716
Mesh size	1.27 mm
Filament diameter	0.25 mm
Hydrodynamic angle	45°

Appendix B. Time and frequency domain of differential pressure signal
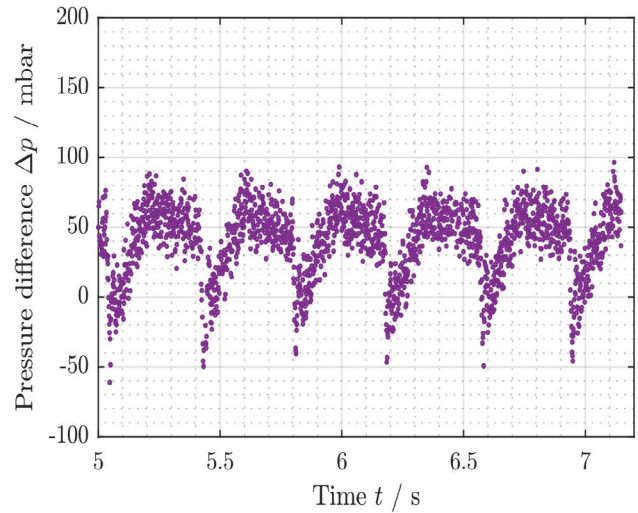

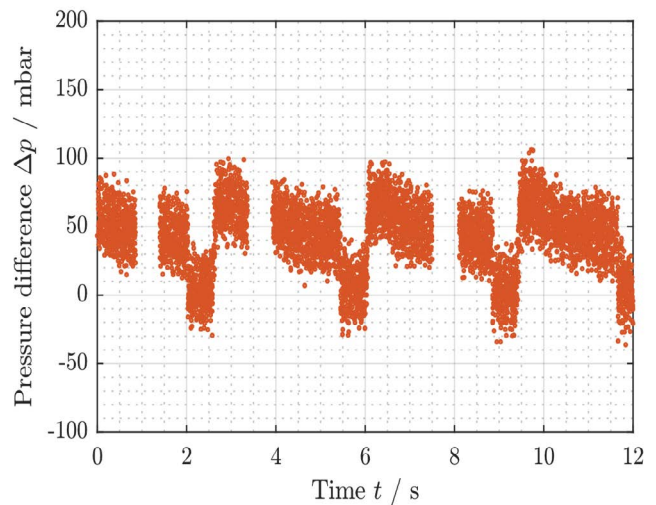Fig. A1. Time domain of differential pressure signal (0.52 Hz).

Fig. A2. Time domain of differential pressure signal (2.65 Hz).

Table A2
Measurement equipment

| Short	Description	Range (calib.)	Error
T_XX	PT1000 4-wire RTD	20°C–100°C	0.1 K
V_1	Magnetic flow meter Optiflux 5100C, DN6 (Krohne Messtechnik GmbH, Duisburg, Germany)	0–200 L/h	0.4% + 1 mm s^{-1}
V_2	Magnetic flow meter Optiflux 5100C, DN4 (Krohne Messtechnik GmbH, Duisburg, Germany)	0–200 L/h	0.4% + 1 mm s^{-1}
P_XX	Pressure sensor A-10 (Wika USA, Lawrenceville, United States)	0–10 bar, abs	0.25% BFSL
P_Diff	Piezo pressure sensor (Keller Ag für Druckmesstechnik, Winterthur, Switzerland)	–0.5 to 0.5 bar, rel	0.2% BFSL
M_F	Scales KMB-TM (Kern & Sohn GmbH, Balingen-Frommern, Germany)	0–6 kg	±0.2 g
M_D	Scales (Sartorius AG, Goettingen, Germany) Combics	0–30 kg	±1 g
C_XX	Conductivity sensor (Jumo GmbH & Co. KG, Fulda, Germany)	0–200 mS cm^{-1}	0.5%
Orifice: Dosch Messapparate GmbH, Berlin, Germany	94D-MBL 500D	1–15 bar	30%–40%
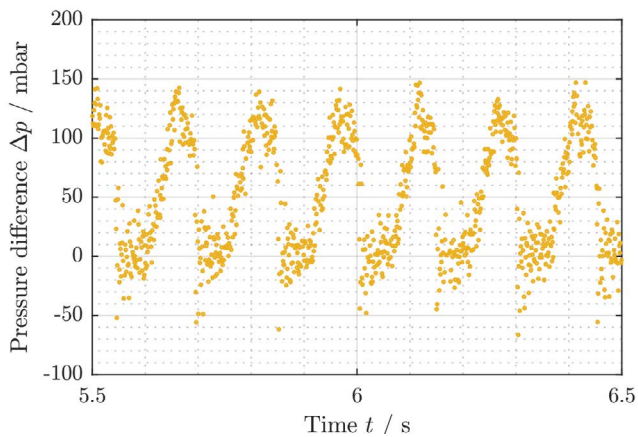
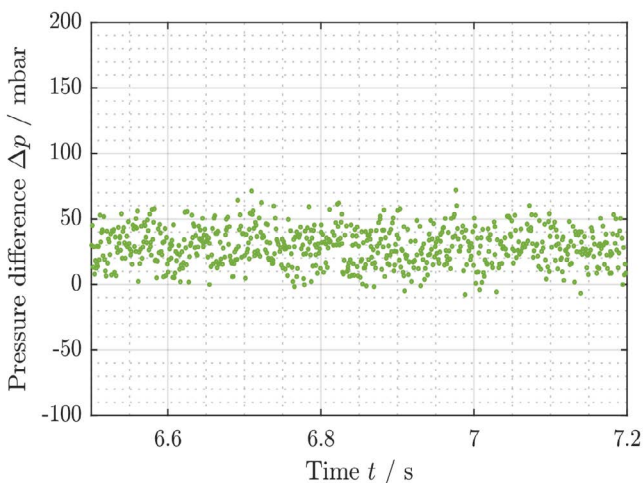Fig. A3. Time domain of differential pressure signal (6.57 Hz).

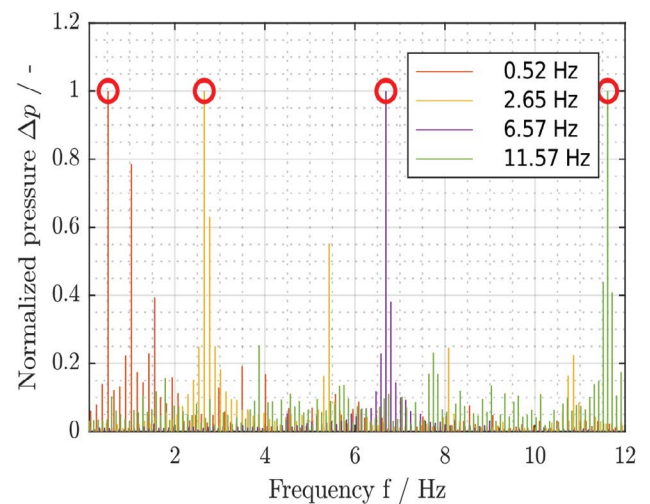Fig. A4. Time domain of differential pressure signal (11.57 Hz).

Fig. A5. Frequency domain of differential pressure signal calculated by fast Fourier transformation. The main frequencies for each pressure signal are marked with a red circle.

Appendix C. Error estimation of the amplitude ratio calculation: deviation due to noisy pressure signals

In this study, the transient differential pressure over an orifice was measured to identify the transient mass flow rate based on the method of Doblhoff-Dier et al. [39]. The study of Doblhoff-Dier et al. [39] solely compared the error of the mean mass flow rate. Therefore, an approximation must be made to estimate the error of the amplitude ratio, which is an important characteristic parameter in pulsating flows. The determination of the transient mass flow rate faces two challenges: The simplification of the Navier–Stokes equations (Eq. (19)) and the measurement error due to the noise of the signal. The error that results of the simplification cannot be given in the scope of this

study, as a reference is missing. Nevertheless, an estimation should be presented and therefore the error of the noise was approximated. The highest value was taken as the mean error of the amplitude ratio to give a conservative estimation.

Therefore, the amplitude ratio was calculated for several frequencies and different SNRs:

$$SNR = 20 \log_{10}\left(\frac{A_{signal}}{A_{noise}}\right) \tag{23}$$

where A_{signal} and A_{noise} represent the amplitude of signal and noise.

- Artificial sinusoidal pressure signals for the frequencies 0.52, 2.57, 6.57, and 11.57 Hz were calculated. Eq. (19) was then used to calculate the transient mass flow rate for all frequencies. The resulting amplitude ratio of the mass flow rate is used as a reference AR_{ref}. The amplitude ratio was calculated with Eq. (4).
- Noise was added to all pressure signals (Fig. A6). The SNR was set to values which were derived from the experimental results.
- Eq. (19) was used to calculate the transient mass flow rate for all signals with varying SNR. For a certain frequency and for a given pressure signal the calculated amplitude ratio of the transient mass flow rate must be the same. Deviations from this can be attributed to the noise added to the sinusoidal pressure signal. The relative deviation $\varepsilon = \dfrac{AR - AR_{ref}}{AR_{ref}}$ from the reference value AR_{ref} is shown in Fig. A7.

Table A3 shows the values of SNR for different frequencies which were derived from the experimentally determined differential pressure measurements over the orifice and the corresponding deviation seen in Fig. A7. The highest deviation of 33.48% appears for the lowest SNR –12.62 dB which represents the highest amount of noise (Eq. (23)).
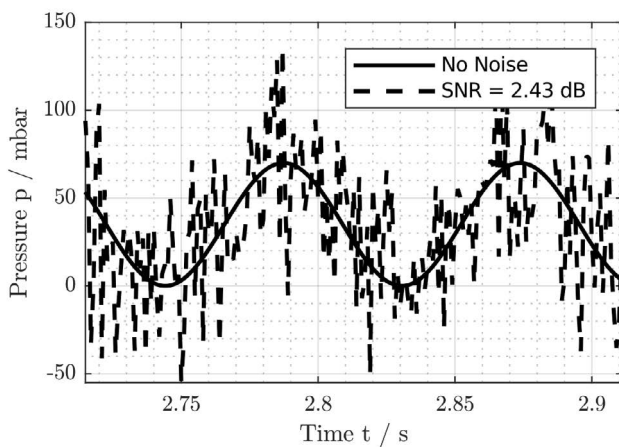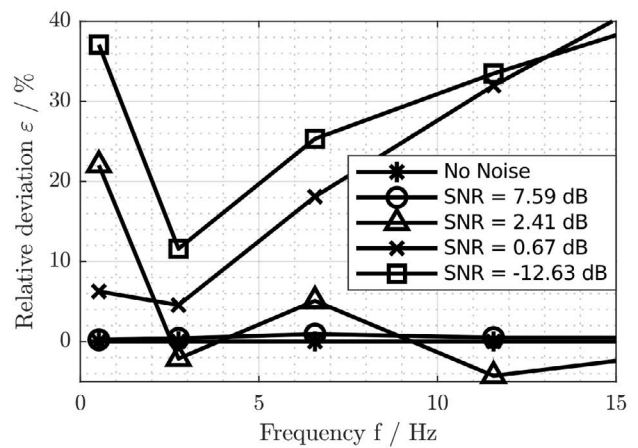
Fig. A7. Relative deviation of amplitude ratio from reference state (no noise) for different signal-to-noise ratios (SNRs).

Table A3
SNR values calculated for the differential pressure measurements and deviation

Frequency (Hz)	SNR (dB)	ε (%)
0.52	0.61	22.04
2.57	7.61	2.75
6.57	2.43	5.09
11.57	–12.62	33.48

Fig. A6. Artificial sinusoidal pressure signal at a frequency of 11.57 Hz with no noise and with a signal-to-noise ratio (SNR) of 2.43 dB.